

Isogeometric Analysis of Acoustic Scattering with Perfectly Matched Layers (IGAPML)

Jon Vegard Venås^{a,*}, Trond Kvamsdal^{b,a}

^a*SINTEF Digital, Mathematics and Cybernetics, 7037 Trondheim, Norway*

^b*Department of Mathematical Sciences, Norwegian University of Science and Technology, 7034 Trondheim, Norway*

Abstract

The perfectly matched layer (PML) formulation is a prominent way of handling radiation problems in unbounded domain and has gained interest due to its simple implementation in finite element codes. However, its simplicity can be advanced further using the isogeometric framework. This work presents a spline based PML formulation which avoids additional coordinate transformation as the formulation is based on the same space in which the numerical solution is sought. The procedure can be automated for any convex artificial boundary. This removes restrictions on the domain construction using PML and can therefore reduce computational cost and improve mesh quality. The usage of spline basis functions with higher continuity also improves the accuracy of the numerical solution.

Keywords:

Isogeometric analysis, acoustic scattering, perfectly matched layers.

1. Introduction

Scattering problems involve *unbounded exterior domains*, Ω^+ (see Figure 1). The use of Boundary Element Method (BEM) is a popular approach for solving such problems [1, 2, 3, 4]. Alternatively, a common approach for solving such problems with the finite element method (FEM) is to introduce an artificial boundary that encloses the scatterer. On the artificial boundary some sort of absorbing boundary condition (ABC) is prescribed. The problem is then reduced to a finite domain, the bounded domain between the scatterer and the artificial boundary can then be discretized with finite elements. Several methods exist for handling the exterior Helmholtz problem (on unbounded domain), including a) the perfectly matched layer (PML) method after Bérenger [5, 6, 7], b) Dirichlet to Neumann-operators (DtN-operators) [8], c) local differential ABC operators [9, 10, 11, 12], and d) the infinite element method (IEM) [13, 14, 15].

In earlier works we have developed isogeometric (IGA) methods [16] for the IEM [17] and the BEM [18] approaches and achieved significant improved accuracy compared to use of C^0 continuous FEM due to the increased inter-element continuity of the splines basis functions.

Regarding IGA for acoustic scatterings most authors have developed methods for BEM. Simpson and coworkers coined the word *IGABEM* for isogeometric methods for BEM in [19] and presented their first paper on IGABEM for acoustic scattering two years later [20]. However, the first paper on isogeometric BEM [21] was published a year before by M. J. Peake during his PhD-study at University of Durham (UK) under supervision of Prof. J. Trevelyan and Prof. G. Coates. Here, the so-called eXtended Isogeometric Boundary Element Method (XIBEM) was introduced and further developed in the two follow up papers [22, 23]. Inspired by these initial papers several investigations of IGABEM applied to acoustics have been pursued by different authors [24, 25, 26, 27, 28, 18, 29]. Recently, acoustic optimization and IGABEM has been pursued with success by a few groups, see e.g., [30, 31, 32, 33, 34, 35, 36, 37, 38].

*Corresponding author.

Email addresses: JonVegard.Venas@sintef.no (Jon Vegard Venås), Trond.Kvamsdal@sintef.no (Trond Kvamsdal)

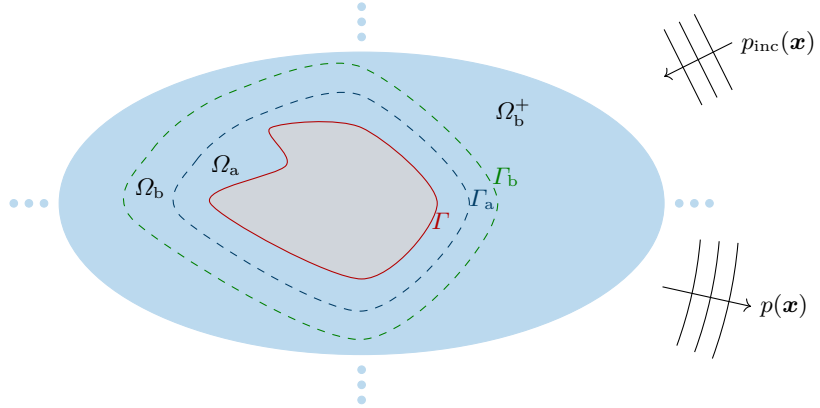


Figure 1: Two convex boundaries Γ_a and Γ_b defines the PML around the scatterer defined by Γ such that the exterior domain Ω^+ is decomposed by the three domains Ω_a (which is bounded by Γ and Γ_a), Ω_b (which is bounded by Γ_a and Γ_b) and Ω_b^+ . Thus, $\Omega^+ = \Omega_a \cup \Omega_b \cup \Omega_b^+$.

The boundary element method (BEM) avoids introducing an artificial boundary as it only relies on a computational domain on the surface of the scatterer. Moreover, solid domains are usually represented by surfaces in CAD-systems, such that if modeling of an elastic scatterer using IGA with the same spline basis as the CAD-model, the BEM does not need a surface-to-volume parametrization. This represents a significant advantage compared to the other approaches regarding interoperability between design and analysis. Thus, the popularity among the IGA community to develop isogeometric methods for BEM (IGABEM) is understandable.

However, we experienced significant challenges related to numerical integration, fictitious eigenfrequencies, and memory requirements and solution times of the resulting algebraic system. These topics are current research areas, and we refer to [39] for references. Furthermore, the frequency spectra of excitation generally have a broad frequency band and thus multi-frequency analysis is often required. Because of the frequency-dependent property, both the traditional BEM and fast multipole BEM must be applied to recalculate all the entries in the system. One way to circumvent the difficulty incurred by acoustic frequency sweeps is to use reduced order models (ROM) [40, 41, 42], but for BEM we must overcome the following two challenges (1) how to construct an orthonormal basis and (2) how to avoid the assembly of system matrices for each frequency before projection. Reduced order modeling of BEM for acoustic scattering is recently addressed in [39] but are still not yet a matured computational methodology.

Thus, use of IGABEM for addressing acoustic scattering is a versatile but challenging computational methodology. In particular, for efficient handling of frequency sweeps by means of reduced order models (ROM) it seems to be of interest to investigate alternative classical isogeometric finite element methods.

The IEM is very efficient for cases where we can locate the artificial boundary close to the scatterer and represent it with ellipsoidal coordinate systems. We developed isogeometric methods for IEM (hereafter denoted *IGAIEM* in [17]¹ and achieved significant improved accuracy compared to use of C^0 continuous FEM. However, in general the need for a surface-to-volume parametrization between the scatterer and the artificial boundary is a disadvantage. Furthermore, we experienced severe challenges with high condition numbers of the system matrix when the number of radial shape functions in the infinite elements is large. This becomes a problem for more complex geometries as the number of radial shape functions must be increased to achieve higher precision. Again, there might be remedies for reducing the conditioning number, see e.g. [43] where this have been addressed for C^0 -Lagrange FE, and that is something we will address in an upcoming paper on *IGAIEM*.

Compared to IEM the PML approach is not prone to ill-conditioning of the system matrix. For most applications the accuracy of the PML is comparable to IEM (for engineering precision; 1% relative error in

¹To the best of our knowledge, our paper seems to be the only one combining isogeometric methods with infinite elements.

energy norm).

Unfortunately, the effective implementation of the PML for convex domains of general shape has not been straight forward because of the geometric parameters that has been required to define the PML-domain. However, Bériot and Modave [44] have recently presented a method for C^0 -Lagrange finite elements that simplifies the implementations significantly. It builds upon the idea of locally conformal PML layers [45, 46]. In the present work we will investigate the use of IGA inspired by this idea to develop what we denote as *IGAPML*. Thus, the IGAPML developed herein enables us to choose the artificial boundary to be an arbitrary convex boundary represented by a NURBS parametrization. That is, we are not restricted to domains defined by the ellipsoidal, cylindrical or Cartesian coordinate system.

In recent papers [47, 48] PML in the isogeometric framework has been presented. The present approach enables a generalization to the NURBS parametrization for the PML layer and considers different stretching functions. The stretching function recommended in the present work not only gives improved results but also reduces the number of PML parameters to tune.

2. Perfectly matched layer (PML) for exterior Helmholtz problems

We partition the unbounded domain Ω^+ into three domains by the boundaries Γ_a and Γ_b ; Ω_a , Ω_b and Ω_b^+ , see Figure 1. Due to the absorbing property of the PML layer, Ω_b , only Ω_a and Ω_b need to be discretized by finite elements.

The exterior Helmholtz problem is given by

$$\nabla^2 p + k^2 p = 0 \quad \text{in } \Omega^+, \quad (1)$$

$$\partial_n p = g \quad \text{on } \Gamma, \quad (2)$$

$$\frac{\partial p}{\partial r} - ikp = o(r^{-1}) \quad \text{with } r = |\mathbf{x}| \quad (3)$$

where the Sommerfeld condition [49] in Eq. (3) restricts the field in the limit $r \rightarrow \infty$ uniformly in $\hat{\mathbf{x}} = \frac{\mathbf{x}}{r}$, such that no waves originate from infinity. The Neumann condition given by the function g will in the case of rigid scattering be given by the incident wave p_{inc} . Zero displacement of the fluid normal on the scatterer (rigid scattering) implies that $\partial_n(p + p_{\text{inc}}) = 0$ where ∂_n denotes the partial derivative in the normal direction on the surface Γ (pointing “out” from Ω^+), which implies that

$$g = -\frac{\partial p_{\text{inc}}}{\partial n}. \quad (4)$$

In this work we consider plane incident waves (with amplitude P_{inc}) traveling in the direction \mathbf{d}_s , which can be written as

$$p_{\text{inc}} = P_{\text{inc}} e^{ik\mathbf{d}_s \cdot \mathbf{x}}. \quad (5)$$

2.1. Far field pattern

The quantity of interest is the *target strength* defined by

$$\text{TS} = 20 \log_{10} \left(\frac{|p_0(\hat{\mathbf{x}})|}{|P_{\text{inc}}|} \right) \quad (6)$$

where the far field pattern of the scattered pressure, p , is given by

$$p_0(\hat{\mathbf{x}}) = \lim_{r \rightarrow \infty} r e^{-ikr} p(r\hat{\mathbf{x}}), \quad (7)$$

with $r = |\mathbf{x}|$ and $\hat{\mathbf{x}} = \mathbf{x}/|\mathbf{x}|$ being the far field observation point. The observation point can be represented in terms of the aspect angle α and elevation angle β

$$\hat{\mathbf{x}} = \begin{bmatrix} \cos \beta \cos \alpha \\ \cos \beta \sin \alpha \\ \sin \beta \end{bmatrix}.$$

We also use this convention in describing the direction of the incident wave

$$\mathbf{d}_s = \begin{bmatrix} \cos \beta_s \cos \alpha_s \\ \cos \beta_s \sin \alpha_s \\ \sin \beta_s \end{bmatrix}.$$

The far field pattern can be computed by (cf. [50], p. 32])

$$p_0(\hat{\mathbf{x}}) = -\frac{1}{4\pi} \int_{\Gamma} \left[ikp(\mathbf{y}) \hat{\mathbf{x}} \cdot \mathbf{n}(\mathbf{y}) + \frac{\partial p(\mathbf{y})}{\partial n(\mathbf{y})} \right] e^{-ik\hat{\mathbf{x}} \cdot \mathbf{y}} d\Gamma(\mathbf{y}). \quad (8)$$

from which the target strength in Eq. (6) may be computed.

2.2. Weak formulation for the Helmholtz equation

The weak formulation is given by (the involved spaces are described in [50])

$$\text{Find } p \in H_w^{1+}(\Omega^+) \text{ such that } B(q, p) = L(q), \quad \forall q \in H_{w^*}^1(\Omega^+), \quad (9)$$

where the bilinear form is given by

$$B(q, p) = \int_{\Omega^+} [\nabla q \cdot \nabla p - k^2 qp] d\Omega$$

and the corresponding linear form is given by

$$L(q) = \int_{\Gamma} q g d\Gamma.$$

2.3. Truly perfectly matched layers

We will here develop a general spline-based (GSB) PML method which avoids intermediate transformation to spherical/cylindrical/Cartesian coordinates. The idea is to construct the spline patches such that the directions we want to have a decaying property is represented by parametric directions of the spline patch. As NURBS can represent spherical and cylindrical patches in addition to the trivial Cartesian patches, it can resolve the standard behavior obtained by the classical PML-formulations using the appurtenant coordinate systems.

The NURBS basis is constructed using B-splines. Therefore, an understanding of B-splines is crucial to understanding NURBS. We extend the classical [51] definition (using the Cox-de Boor formula) to evaluations in the complex parametric space as follows. Let \check{p} be the polynomial order², let n be the number of basis functions and define a *knot vector* $\mathbf{t} = \{\xi_1, \xi_2, \dots, \xi_{n+\check{p}+1}\}$ to be an ordered vector with non-decreasing elements, called *knots*. Then, the n B-splines, $\{B_{i,\check{p},\mathbf{t}}\}_{i \in [1,n]}$, are recursively defined by

$$B_{i,\check{p},\mathbf{t}}(\xi) = \frac{\xi - \xi_i}{\xi_{i+\check{p}} - \xi_i} B_{i,\check{p}-1,\mathbf{t}_1}(\xi) + \frac{\xi_{i+\check{p}+1} - \xi}{\xi_{i+\check{p}+1} - \xi_{i+1}} B_{i+1,\check{p}-1,\mathbf{t}_1}(\xi)$$

starting with (the only alteration to the classical Cox-de Boor formula is that we here take the real part of the parameter ξ)

$$B_{i,0,\mathbf{t}_1}(\xi) = \begin{cases} 1 & \text{if } \xi_i \leq \text{Re } \xi < \xi_{i+1} \\ 0 & \text{otherwise.} \end{cases} \quad (10)$$

²The usage of a check sign above the polynomial order p is to avoid ambiguity between the polynomial order and the scattered pressure.

With B-splines in our arsenal, we are ready to present Non-Uniform Rational B-Splines (NURBS). Let $\{w_i\}_{i \in [1, n]}$ be a set of *weights*, and define the *weighting function* by

$$W(\xi) = \sum_{\tilde{i}=1}^n B_{\tilde{i}, \check{p}, \mathbf{t}}(\xi) w_{\tilde{i}}.$$

The one-dimensional NURBS basis functions can now be defined by

$$R_i(\xi) = \frac{B_{i, \check{p}, \mathbf{t}}(\xi) w_i}{W(\xi)}.$$

The extensions to bivariate NURBS surfaces and trivariate NURBS volumes are straightforward. For NURBS volumes, let $\{B_{i_1, \check{p}_1, \mathbf{t}_1}\}_{i_1 \in [1, n_1]}$, $\{B_{i_2, \check{p}_2, \mathbf{t}_2}\}_{i_2 \in [1, n_2]}$ and $\{B_{i_3, \check{p}_3, \mathbf{t}_3}\}_{i_3 \in [1, n_3]}$ be the sets of B-spline basis functions in ξ_1 -, ξ_2 - and ξ_3 -direction, respectively. These sets have their own order (\check{p}_1 , \check{p}_2 and \check{p}_3 , respectively) and knot vectors (\mathbf{t}_1 , \mathbf{t}_2 and \mathbf{t}_3 , respectively). The trivariate NURBS basis functions are then defined by

$$R_{i_1, i_2, i_3}(\xi_1, \xi_2, \xi_3) = \frac{B_{i_1, \check{p}_1, \mathbf{t}_1}(\xi_1) B_{i_2, \check{p}_2, \mathbf{t}_2}(\xi_2) B_{i_3, \check{p}_3, \mathbf{t}_3}(\xi_3) w_{i_1, i_2, i_3}}{W(\xi_1, \xi_2, \xi_3)} \quad (11)$$

where the weighting function is now given by

$$W(\xi_1, \xi_2, \xi_3) = \sum_{\tilde{i}_1=1}^{n_1} \sum_{\tilde{i}_2=1}^{n_2} \sum_{\tilde{i}_3=1}^{n_3} B_{\tilde{i}_1, \check{p}_1, \mathbf{t}_1}(\xi_1) B_{\tilde{i}_2, \check{p}_2, \mathbf{t}_2}(\xi_2) B_{\tilde{i}_3, \check{p}_3, \mathbf{t}_3}(\xi_3) w_{\tilde{i}_1, \tilde{i}_2, \tilde{i}_3}.$$

A NURBS patch can be represented by the transformation

$$\mathbf{X} : [0, 1]^3 \rightarrow \Omega_b \subset \mathbb{R}^3, \quad (\xi_1, \xi_2, \xi_3) \mapsto \sum_{i_1=1}^{n_1} \sum_{i_2=1}^{n_2} \sum_{i_3=1}^{n_3} R_{i_1, i_2, i_3}(\xi_1, \xi_2, \xi_3) \mathbf{P}_{i_1, i_2, i_3} \quad (12)$$

with $\mathbf{P}_{i_1, i_2, i_3}$ being the control points of the patch. For brevity the PML formulation will be derived for a single NURBS patch representing Ω_b , but the generalization to a multipatch representation is straight forward. Without loss of generalization, we have here assumed normalized knots in the patch in which we want the PML transformation.

The complex coordinate transformation representing the PML coordinate stretching is given by

$$\mathbf{S} : [0, 1]^3 \rightarrow \mathbb{C}^3, \quad (\xi_1, \xi_2, \xi_3) \mapsto \mathbf{S}(\xi_1, \xi_2, \xi_3) = (\tilde{\xi}_1, \tilde{\xi}_2, \tilde{\xi}_3) \quad (13)$$

where

$$\tilde{\xi}_i = \xi_i + i I_i(\xi_i), \quad I_i(\xi_i) = \int_0^{\xi_i} \sigma_i(\xi) d\xi \quad (14)$$

and σ_i is a monotonically increasing functions satisfying $\sigma_i \geq 0$.

Instead of using the bilinear form defined in the physical space ($\mathbf{x} \in \Omega^+ \subset \mathbb{R}^3$), we use the bilinear form over the space $\tilde{\Omega}^+ = \{\mathbf{T}(\mathbf{x}) : \mathbf{x} \in \Omega^+\}$ where

$$\mathbf{T} : \mathbb{R}^3 \rightarrow \mathbb{C}^3, \quad \tilde{\mathbf{x}} = \mathbf{T}(\mathbf{x}) = \mathbf{X}(\mathbf{S}(\mathbf{X}^{-1}(\mathbf{x}))). \quad (15)$$

The bilinear form is then given by

$$B(p, q) = \int_{\tilde{\Omega}^+} \tilde{\nabla} q \cdot \tilde{\nabla} p - k^2 qp d\tilde{\Omega}. \quad (16)$$

We then need the Jacobian matrix, $\tilde{\mathbf{J}} = \frac{\partial \mathbf{x}}{\partial \tilde{\mathbf{x}}}$, in order to compute $\tilde{\nabla} p = \nabla p \tilde{\mathbf{J}}$. Applying the chain rule (with $\mathbf{J} = \frac{\partial \mathbf{X}}{\partial \xi}$ and $\mathbf{D} = \frac{\partial \tilde{\xi}}{\partial \xi} = \mathbf{I} + i \operatorname{diag}(\sigma_1(\xi_1), \sigma_2(\xi_2), \sigma_3(\xi_3))$) yields

$$\nabla p = \tilde{\nabla} p \mathbf{J}_{\text{PML}}, \quad \mathbf{J}_{\text{PML}} = \frac{\partial \tilde{\mathbf{X}}}{\partial \tilde{\xi}} \frac{\partial \tilde{\xi}}{\partial \xi} \frac{\partial \xi}{\partial \mathbf{X}} = \mathbf{J}(\tilde{\xi}) \mathbf{D}(\xi) \mathbf{J}^{-1}(\mathbf{x}). \quad (17)$$

Since $\nabla p \mathbf{J}(\boldsymbol{\xi}) = \nabla_{\boldsymbol{\xi}} p$ we have $\tilde{\nabla} p = \nabla_{\boldsymbol{\xi}} p \mathbf{D}^{-1} \mathbf{J}(\tilde{\boldsymbol{\xi}})^{-1}$, which inserted into the bilinear form yields (for a single patch)

$$B(p, q) = \int_{[0,1]^3} [(\mathbf{J}(\tilde{\boldsymbol{\xi}})^{-\top} \mathbf{D}^{-1} \nabla_{\boldsymbol{\xi}}^\top q) \cdot (\mathbf{J}(\tilde{\boldsymbol{\xi}})^{-\top} \mathbf{D}^{-1} \nabla_{\boldsymbol{\xi}}^\top p) - k^2 qp] \det(\mathbf{J}(\tilde{\boldsymbol{\xi}})) \det(\mathbf{D}) d\boldsymbol{\xi}. \quad (18)$$

This reduces to the standard bilinear form whenever $\sigma_i = 0, \forall i$. Compare this bilinear form to the bilinear form for spherical coordinates, (r, ϑ, φ) in [52]

$$B(p, q) = \int_{[0,1]^3} [(\mathbf{J}_s^{-\top} \mathbf{D}^{-1} \mathbf{J}_s^\top \mathbf{J}^{-\top} \nabla_{\boldsymbol{\xi}}^\top q) \cdot (\mathbf{J}_s^{-\top} \mathbf{D}^{-1} \mathbf{J}_s^\top \mathbf{J}^{-\top} \nabla_{\boldsymbol{\xi}}^\top p) - k^2 qp] \det(\mathbf{J}) \det(\mathbf{D}) d\boldsymbol{\xi} \quad (19)$$

where

$$\mathbf{J}_s = \begin{bmatrix} \sin \vartheta \cos \varphi & r \cos \vartheta \cos \varphi & -r \sin \vartheta \sin \varphi \\ \sin \vartheta \sin \varphi & r \cos \vartheta \sin \varphi & r \sin \vartheta \cos \varphi \\ \cos \vartheta & -r \sin \vartheta & 0 \end{bmatrix}, \quad \mathbf{D} = \mathbf{I} + i \operatorname{diag} \left(\sigma(\xi), \frac{1}{r} I(\xi), \frac{1}{r} I(\xi) \right) \quad (20)$$

with $\xi = \frac{r-R}{S-R}$. In the present formulation the evaluation of trigonometric functions in the assembly procedure is therefore replaced by NURBS-evaluations.

In [52], the following decay function is used

$$\sigma(\xi) = \xi(e^{\gamma\xi} - 1) \quad (21)$$

which gives

$$I(\xi) = \frac{e^{\gamma\xi}(\gamma\xi - 1) + 1}{\gamma^2} - \frac{\xi^2}{2}. \quad (22)$$

This would require finding γ for each setup as it would be depending on the frequency and the PML thickness. Alternatively, the following decay function may be used [53, 54, 47]

$$\sigma(\xi) = -\gamma\xi^n \ln \epsilon, \quad n = 2 \quad (23)$$

which gives

$$I(\xi) = -\frac{\gamma}{n+1} \xi^{n+1} \ln \epsilon. \quad (24)$$

In [55, 56] a decay function with unbounded integral was shown to be optimal with the assumption of Dirichlet boundary conditions at Γ_b . The following function

$$\sigma(\xi) = \gamma(1 - \xi)^{-n}, \quad 1 \leq n < 3 \quad (25)$$

with

$$I(\xi) = \begin{cases} \gamma \frac{(1-\xi)^{1-n}-1}{n-1} & n > 1 \\ -\gamma \ln(1 - \xi) & n = 1 \end{cases} \quad (26)$$

was found to be optimal for $n = 1$ and $\gamma = \frac{1}{k_{\text{PML}}^2}$ (translated for the present PML formulation) for 2D acoustic scattering. Unless otherwise stated, this function will be used in the examples herein. As noted in [55] this function yields discontinuity at $\xi = 0$. Somewhat surprisingly the continuous alternative

$$\sigma(\xi) = \gamma[(1 - \xi)^{-n} - 1], \quad 1 \leq n < 3 \quad (27)$$

with

$$I(\xi) = \begin{cases} \gamma \left[\frac{(1-\xi)^{1-n}-1}{n-1} - \xi \right] & n > 1 \\ -\gamma[\ln(1 - \xi) + \xi] & n = 1 \end{cases} \quad (28)$$

did not give better results.

Consider a plane wave at the far side of the PML where the PML (between $0 < x_3 < t_{\text{PML}}$) is parameterized by $\mathbf{X} = \xi_1 \mathbf{e}_1 + \xi_2 \mathbf{e}_2 + t_{\text{PML}} \xi_3 \mathbf{e}_3$

$$p_{\text{inc}}(\tilde{\mathbf{x}})|_{\tilde{\Gamma}_b} = P_{\text{inc}} e^{i\mathbf{k} \cdot \tilde{\mathbf{x}}} = P_{\text{inc}} e^{i\mathbf{k} \cdot \mathbf{x}} e^{-k_3 t_{\text{PML}} I(1)}. \quad (29)$$

If we want $|p_{\text{inc}}/P_{\text{inc}}|$ to decay to a value ϵ at Γ_b we must have

$$\epsilon = e^{-k_3 t_{\text{PML}} I(1)}. \quad (30)$$

For the particular function in Eq. (23) we can compute γ to be

$$\gamma = \frac{n+1}{k_3 t_{\text{PML}}}. \quad (31)$$

Whenever Γ_a is a smooth convex surface we can construct the NURBS patches representing the PML by first finding a NURBS parametrization $\mathbf{X}_b(\xi_1, \xi_2)$ which is a distance t_{PML} away from $\mathbf{X}_a(\xi_1, \xi_2)$ (achieved by minimizing $\mathbf{X}_b - \mathbf{X}_a - t_{\text{PML}} \mathbf{n}_a$ where \mathbf{n}_a is the normal vector at \mathbf{X}_a) and then computing a linear lofting between \mathbf{X}_a and \mathbf{X}_b to obtain the volumetric NURBS patches.

The present approach of defining the PML stretching function directly on the NURBS parametric space differs from the Automatic Matched Layer (AML) in [44] where the stretching coordinate is based on the distance to the artificial boundary $\mathbf{X}_a \in \Gamma_a$ through $r(\xi) = \text{dist}(\Gamma_a, \mathbf{X}(\xi)) = \|\mathbf{X}(\xi) - \mathbf{X}_a(\xi)\|$ where the decay is defined in the direction

$$\mathbf{n}(\xi) = \frac{\mathbf{X}(\xi) - \mathbf{X}_a(\xi)}{\|\mathbf{X}(\xi) - \mathbf{X}_a(\xi)\|}.$$

However, unless the NURBS patches are constructed such that $\text{dist}(\Gamma_a, \mathbf{X}(\xi)) = t_{\text{PML}} \xi_1$ (assuming ξ_1 is the decay direction) we would in general have slightly different decay directions, that is,

$$\mathbf{n}(\xi) \neq \frac{\frac{\partial \mathbf{X}(\xi)}{\partial \xi_1}}{\left\| \frac{\partial \mathbf{X}(\xi)}{\partial \xi_1} \right\|} \quad (32)$$

and thus the convenient formula for the Jacobian [44, Eq. (25)] cannot in general be used as suggested in [47, Eq. (21)] (according to our understanding of their approach). The difference is that $\mathbf{X}_a(\xi_1, \xi_2, \xi_3) \neq \mathbf{X}(0, \xi_2, \xi_3)$. We must use the approach outlined above, or assume that the NURBS patches have the parameter representing the decay directed normally from Γ_a for all points. The construction of such patches is however not necessarily possible in terms of NURBS basis functions, even for smooth surfaces Γ_a . Alternatively, the AML approach can be used for the NURBS parametrization but then time consuming Newton iterations for finding \mathbf{X}_a would be required for all quadrature points in Ω_b . A way to resolve this could be to precompute all these points. The disadvantage of the approach outlined above is the complex evaluations of the NURBS basis functions through the extended definition in Eq. (10), where the concern is mainly the computational efficiency (not so much the implementation aspect). The most computationally efficient approach is suggested as a future study.

3. Numerical examples

We initiate this section with an investigation on a sphere where analytic solution exists to the plane wave scattering problem. Then, we consider a manufactured solution on a cylindrical domain, before ending with a scattering problem on a more complex geometry.

3.1. Scattering from rigid sphere

We start by performing the same analysis done in Figure 9 in [17] were the convergence through h -refinement is studied on a rigid scattering problem on a sphere of radius $R = 5.075$ m. For completeness the mesh construction is here repeated. The meshes will be generated from a standard discretization of a sphere using NURBS as seen in fig. 2. We shall denote by $\mathcal{M}_{m, \check{p}, \check{k}}^{\text{IGAPML}}$, mesh number m with polynomial order \check{p} and continuity \check{k} across element boundaries³. For the corresponding FEM meshes we denote by $\mathcal{M}_{m, \check{p}, s}^{\text{FEMPML}}$ and

³Except for some possible C^0 interfaces in the initial CAD geometry.

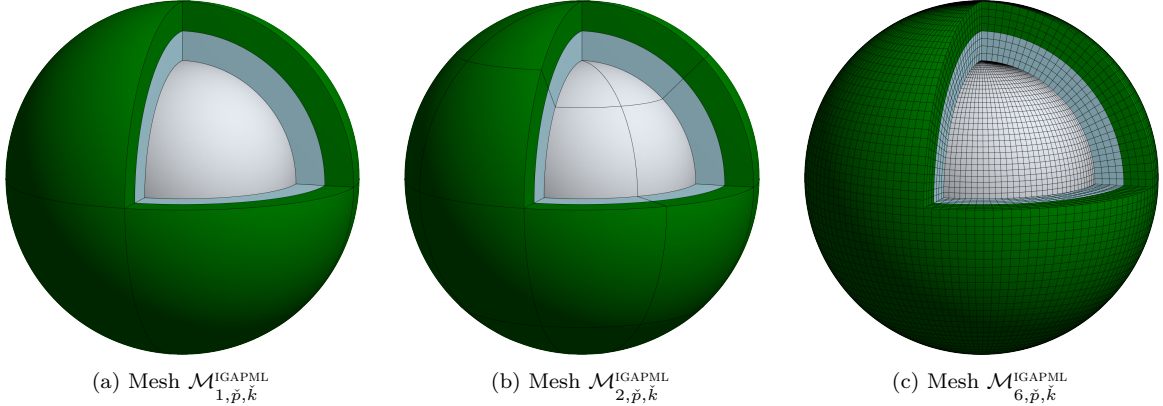


Figure 2: **Scattering from rigid sphere:** Illustration of the coarse mesh $\mathcal{M}_{1,\check{p},\check{k}}^{\text{IGAPML}}$ and the first and fifth refinement. The PML domain (green) has the same thickness as the domain inside Γ_a (in light blue) which is attached to the spherical (grey) scatterer, Γ .

$\mathcal{M}_{m,\check{p},i}^{\text{FEMPML}}$ the subparametric and isoparametric FEM meshes, respectively. The initial mesh is depicted as mesh $\mathcal{M}_{1,\check{p},\check{k}}^{\text{IGAPML}}$ in fig. 2a and is refined only in the angular directions for the first 3 refinements (that is, mesh $\mathcal{M}_{4,\check{p},\check{k}}^{\text{IGAPML}}$ only have two element thickness in the radial direction). Mesh $\mathcal{M}_{m,\check{p},\check{k}}^{\text{IGAPML}}$, $m = 5, 6$, have 4 and 8 elements in the radial direction, respectively. This is done to obtain low aspect ratios for the elements. All the meshes will then be nested and the refinements are done uniformly. We shall use the same polynomial order in all parameter directions; $\check{p}_\xi = \check{p}_\eta = \check{p}_\zeta$. The $\mathcal{M}_{m,\check{p},\check{k}}^{\text{IGAIE}}$ meshes used in [17] correspond to the light blue domain in fig. 2 (with the PML-layer being replaced by infinite elements).

The energy norm is here defined by (cf. [17])

$$\|p\|_{\Omega_a} = \sqrt{\int_{\Omega_a} |\nabla p|^2 + k^2 |p|^2 \, d\Omega}. \quad (33)$$

Figure 3 illustrates the same story as observed in [17]; The increased continuity of the basis functions offered by IGA play a crucial role for improving the accuracy of the numerical solution. To obtain higher accuracy using PML it is however important to know that the PML-thickness influences the accuracy as illustrated in fig. 4. This in turn increases dofs used in order to maintain the aspect ratio of the elements. This problem is here not prevalent for the IEM [17]. Before pollution from the PML-thickness becomes dominant we see that the PML approximation yields solution close to the best approximation. Finally, a comparison between two stretching functions are made in fig. 5. The stretching function in Eq. (25) gives much better results than that of Eq. (23). The PML simulation with the doubled PML thickness again follows closely the best approximation (here in the $L^2(\Gamma)$ -norm).

3.2. Cylinder

In fig. 9 we motivate the implementation of the Combined Helmholtz Integral Formulation [57] (CHIEF) on the Collocation Conventional Boundary Integral Equation (CCBIE) [18] formulation (named CCBIEC) which will be used to make a reference solution for this section.

Consider a cylinder⁴ of length $L = \pi$ m and radius $R = 1$ m centered at the origin with domain

$$\Omega^- = \left\{ \mathbf{x} \in \mathbb{R} : x_1^2 + x_2^2 \leq R^2 \quad \text{and} \quad -\frac{L}{2} \leq x_3 \leq \frac{L}{2} \right\}.$$

Its interior Dirichlet problem ($p(\mathbf{x}) = 0$, $\mathbf{x} \in \partial\Omega^-$) has eigenfunctions⁵ (cf. [58, p. 52])

⁴Note that the experimental simulation herein rotates the cylinder to be aligned with the x -axis. The eigenfrequencies are not altered by this transformation.

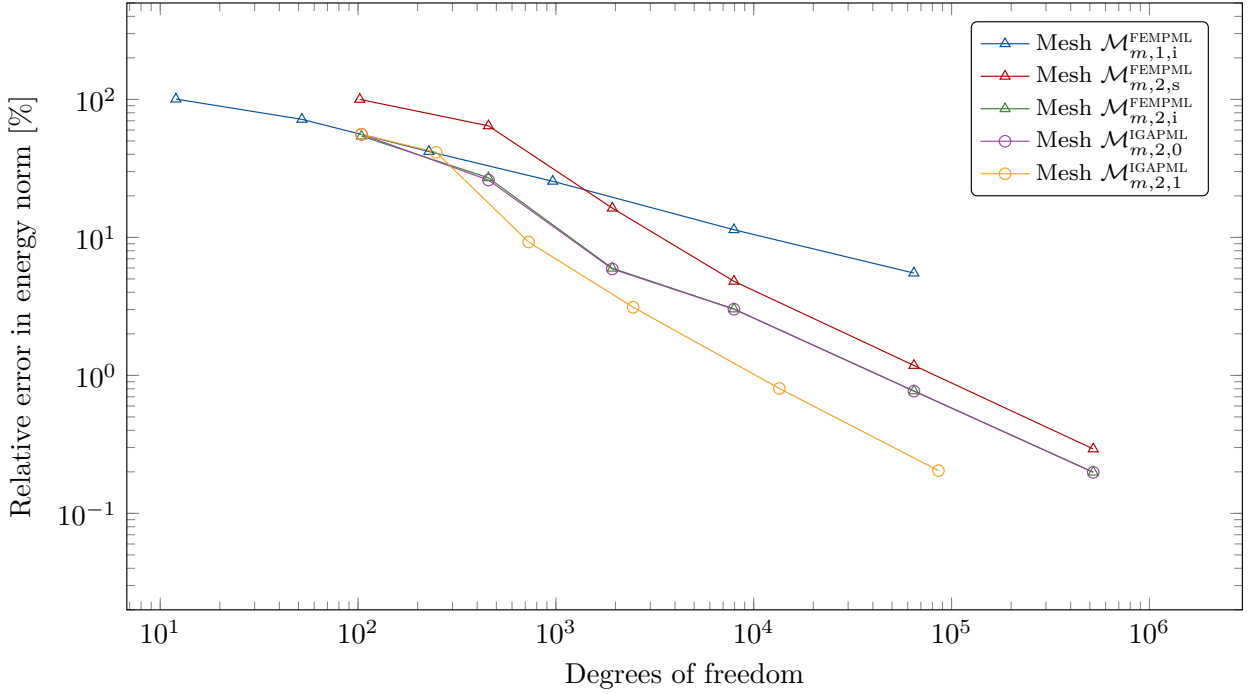


Figure 3: **Scattering from rigid sphere:** Convergence analysis on the rigid scattering case with $kR = 5.075$ and mesh $\mathcal{M}_{m,2,1}$, $m = 1, \dots, 6$. For the PML formulation the stretching function in Eq. (25) is used with $n = 1$. The relative energy error (from Eq. (33)) is plotted against the degrees of freedom.

$$p(\mathbf{x}) = \sin \frac{n_3 \pi (x_3 + L/2)}{L} J_n \left(\frac{x_{nm}^*}{R} r \right) \cos n\theta, \quad n_3 \in \mathbb{N}^*, \quad J_n(x_{nm}^*) = 0, \quad \mathbf{x} \in \Omega^-$$

where

$$k = \sqrt{\left(\frac{x_{nm}^*}{R} \right)^2 + \left(\frac{n_3 \pi}{L} \right)^2},$$

where x_{nm}^* excludes the trivial solutions ($x_{nm}^* \neq 0$) and the interior Neumann problem ($\partial_n p(\mathbf{x}) = 0$, $\mathbf{x} \in \partial\Omega^-$) has eigenfunctions

$$p(\mathbf{x}) = \cos \frac{n_3 \pi (x_3 + L/2)}{L} J_n \left(\frac{x_{nm}}{R} r \right) \cos n\theta, \quad n_3 \in \mathbb{N}, \quad J'_n(x_{nm}) = 0, \quad \mathbf{x} \in \Omega^-$$

where

$$k = \sqrt{\left(\frac{x_{nm}}{R} \right)^2 + \left(\frac{n_3 \pi}{L} \right)^2}.$$

For the exterior problem these eigenfrequencies correspond to the fictitious eigenfrequencies for the CBIE (conventional boundary integral equation) formulation and the HBIE (hyper-singular boundary integral equation) formulation, respectively. The fictitious eigenfrequencies below $kL = 15$ are given by

$$kL \approx 8.182137, 9.826300, 12.079081, 12.440854, 13.578794, 14.662586 \quad (34)$$

for the CBIE formulation, and

$$kL \approx 0, \pi, 5.784249, 2\pi, 6.582336, 8.540255, 3\pi, 9.595168, 10.096379, 11.058209, 11.469336, 12.037659, 12.440854, 4\pi, 13.198424, 13.449673, 13.567167, 13.578794, 13.833698, 14.617689 \quad (35)$$

⁵Here, J_n is the cylindrical Bessel function of the first type.

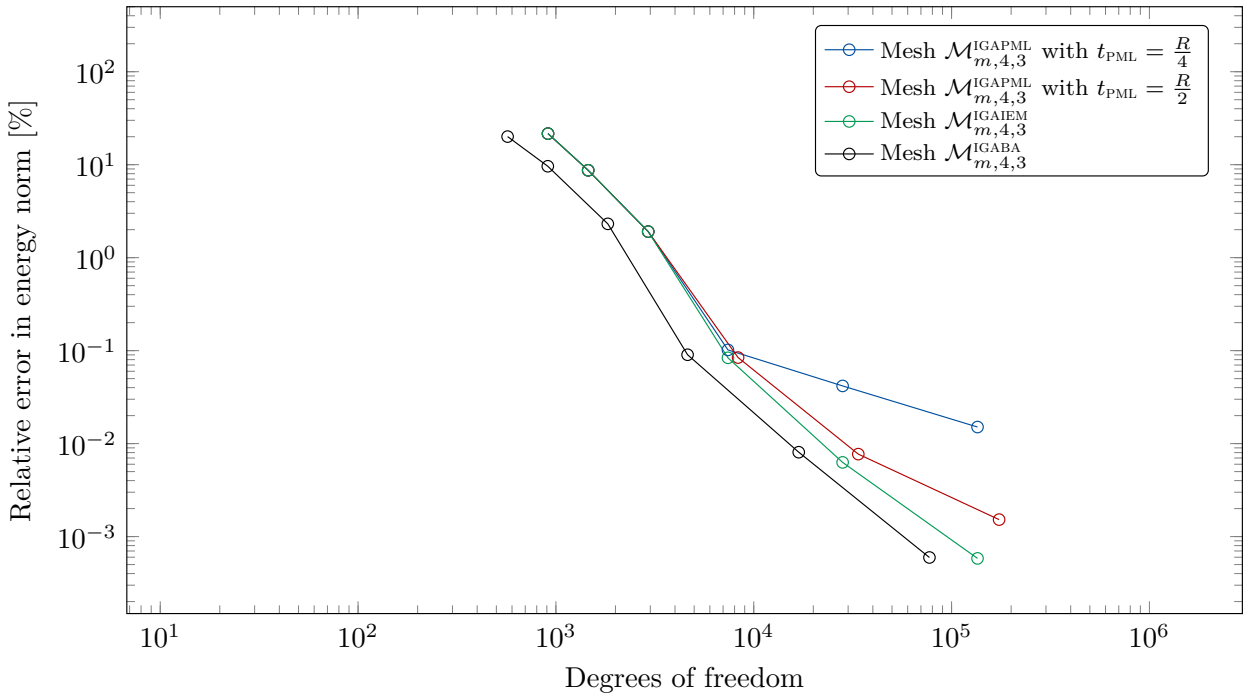


Figure 4: **Scattering from rigid sphere:** Convergence analysis on the rigid scattering case with $kR = 5.075$ and mesh $\mathcal{M}_{m,4,3}$, $m = 1, \dots, 6$. For the PML formulation the stretching function in Eq. (25) is used with $n = 1$. The relative energy error (from Eq. (33)) is plotted against the degrees of freedom. When doubling the PML thickness we also double the number of elements in the radial direction (which can be seen by an increase of dofs used in the final three meshes). The best approximation (BA) is in the L^2 -norm over the domain Ω_a . Note that the best approximation simulation lacks elements in Ω_b and its curve is here thus shifted to the left. With increased PML thickness the PML-simulations converge to the accuracy of the IEM-simulations.

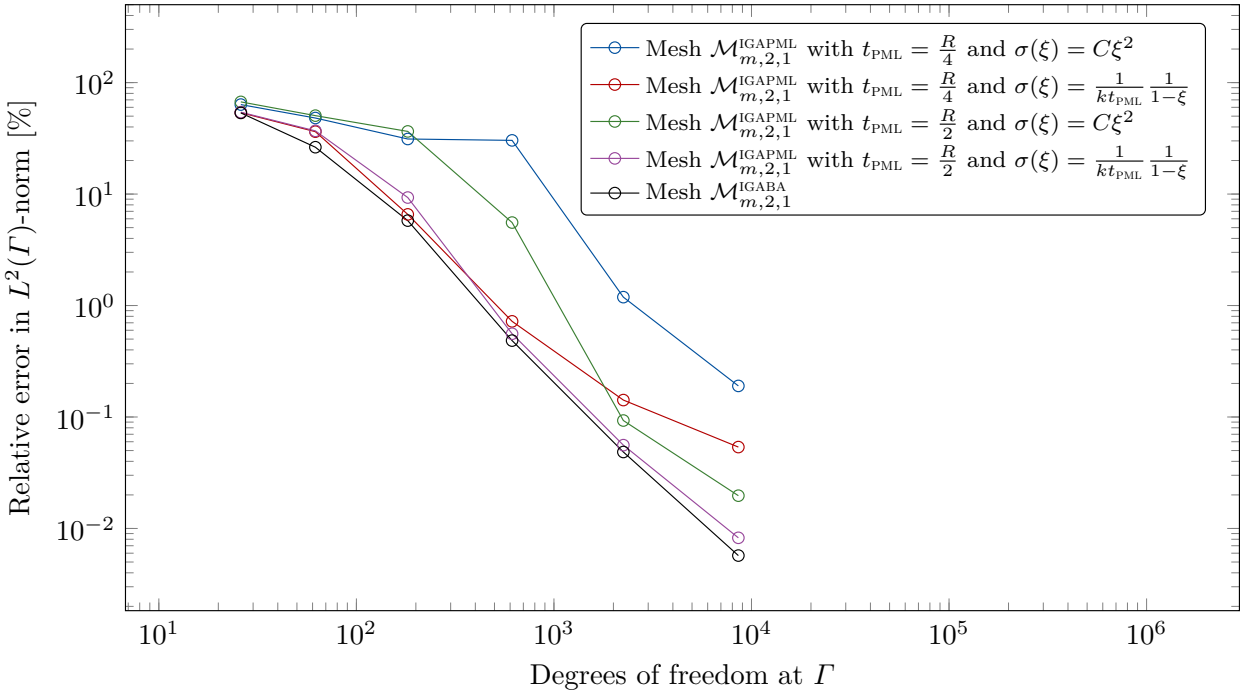


Figure 5: **Scattering from rigid sphere**: Convergence analysis on the rigid scattering case with $kR = 5.075$ and mesh $\mathcal{M}_{m,4,3}$, $m = 1, \dots, 6$. The relative L^2 -error is plotted against the degrees of freedom. The two stretching functions used here are given in Eqs. (23) and (25), respectively. Here, $C = \alpha/(knt_{\text{PML}}^{n-1})$ with $\alpha = 30$ and $n = 2$. Note that $\alpha = 30$ was used instead of $\alpha = 10$ as in [47] as the former gave much better results. The best approximation (BA) is for the degrees of freedom at Γ in the L^2 -norm.

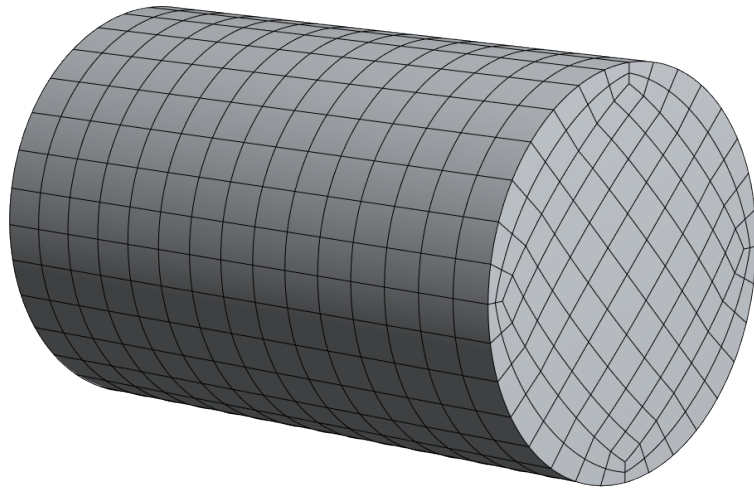
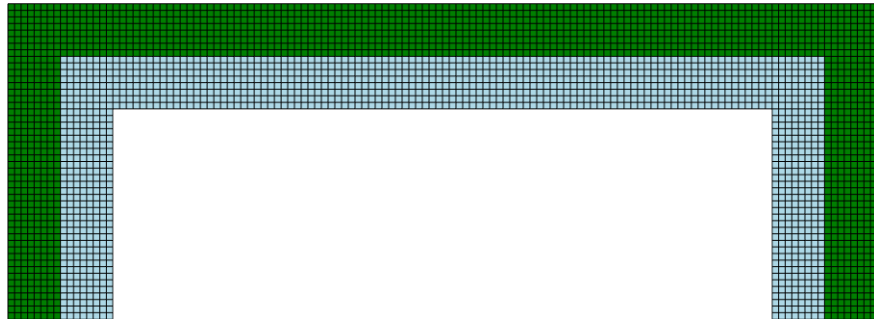
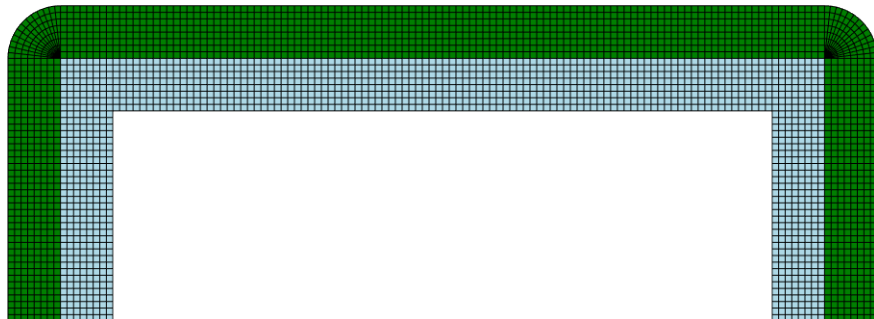


Figure 6: **Cylinder**: Boundary element method mesh $\mathcal{M}_{4,2,1}^{\text{IGABEM}}$ (with 736 elements and 956 degrees of freedom).



(a) A xz -cross sectional of mesh $\mathcal{M}_{6,2,1}^{\text{PML}}$ (with 912 576 elements and 1 058 544 degrees of freedom).



(b) A xz -cross sectional of mesh $\tilde{\mathcal{M}}_{6,\tilde{p},\tilde{k}}^{\text{PML}}$ (with 936 096 elements and 1 082 304 degrees of freedom).

Figure 7: **Cylinder**: Two cross sectional meshes that can be revolved around the x -axis (tensorially with a NURBS representation of a circle) to obtain the volumetric mesh used with the PML approach (i.e. fig. 8). The PML domain is here highlighted in green. The meshes are constructed in a way that optimizes the aspect ratio.

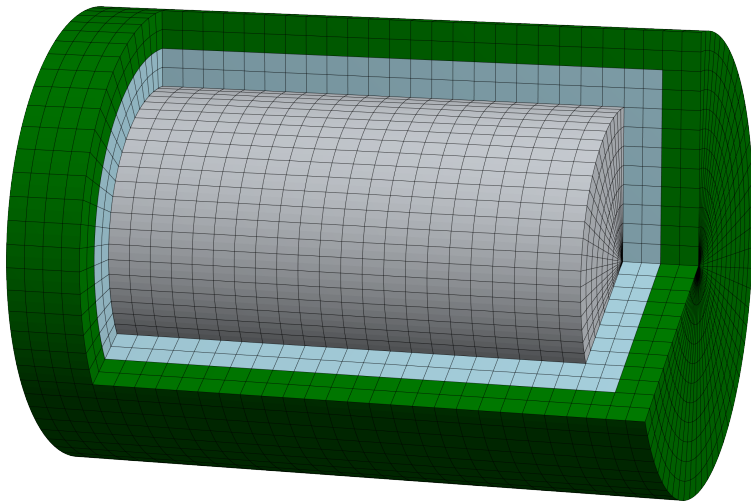


Figure 8: **Cylinder**: PML mesh $\mathcal{M}_{4,2,1}^{\text{IGAPML}}$ (with 12144 elements and 20712 degrees of freedom).

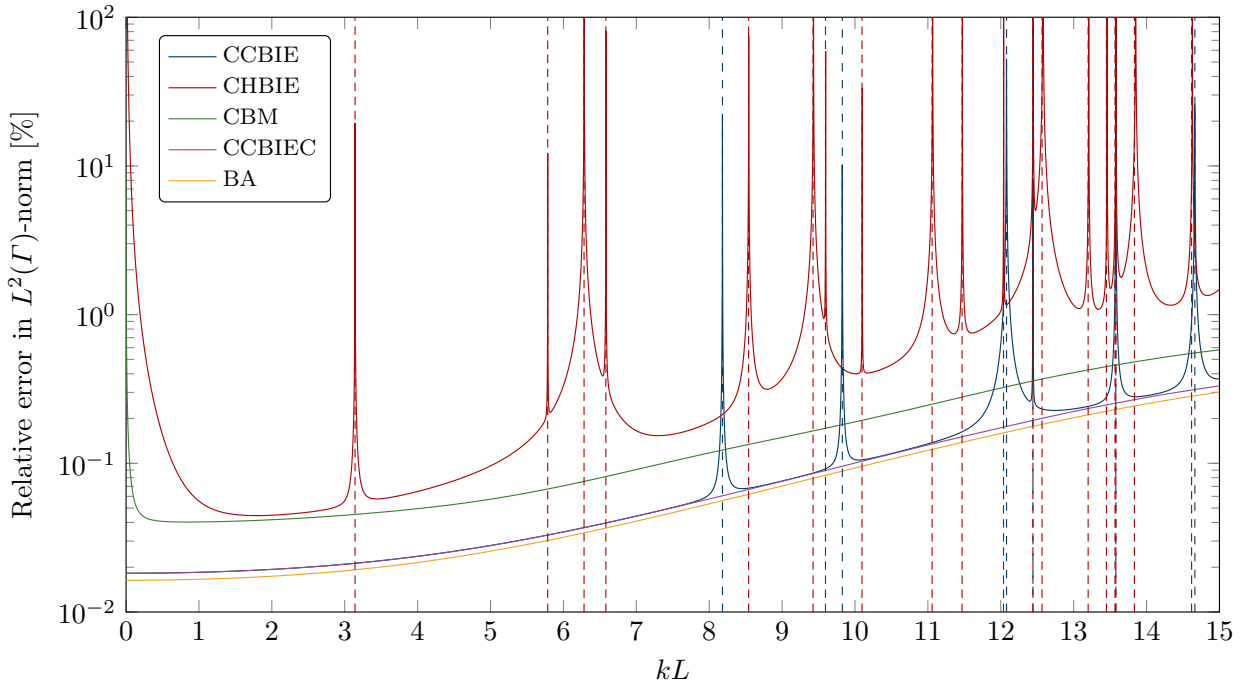


Figure 9: **Manufactured solution with a cylinder:** The plots show the instabilities around eigenfrequencies of the corresponding interior Dirichlet problem using IGABEM formulations [18]. All computations are done using the parametrization in fig. 6 with NURBS degree 2. The dashed lines correspond to the fictitious eigenfrequencies in Eqs. (34) and (35).

for the HBIE formulation.

Consider the manufactured solution (cf. [18])

$$p(\mathbf{x}) = \sum_{n=1}^N C_n \Phi_k(\mathbf{x}, \mathbf{y}_n), \quad \Phi_k(\mathbf{x}, \mathbf{y}) = \frac{e^{ikR}}{4\pi R}, \quad \text{where} \quad R = |\mathbf{x} - \mathbf{y}| \quad \text{and} \quad C_n = \cos(n - 1). \quad (36)$$

with $N = 3^3 = 27$ source points

$$\mathbf{y}_n = \frac{R}{4}[c_i, c_j, c_l], \quad n = i + 3(j - 1) + 3^2(l - 1), \quad i, j, l = 1, 2, 3$$

where $c_1 = -1$, $c_2 = 0$ and $c_3 = 1$. A total of $4^3 = 64$ uniformly spaced points around the origin on a regular cube grid of side length $1/4$ is used for the interior points in the CHIEF formulation. The results are given in fig. 9 where we can see that the CCBIEC formulation follows the best approximation (BA) throughout the frequency sweep without any fictitious eigenfrequencies present in the CCBIE and CHBIE formulations. The CBM (collocation Burton-Miller) formulation removes the fictitious frequencies but has a reduces accuracy compared to the CCBIEC formulation. Consider now the same cylinder scattering a plane wave incident with the x -direction. Some PML meshes are found in fig. 7 where two meshing strategies are outlined. Both strategies yields roughly the same accuracy. The possibility to fill corners like this will be important to create an automatic PML mesh generator for non-smooth artificial boundary as in this example. The near-field is plotted in fig. 10 (for $k = 100 \text{ m}^{-1}$) and the far field (for $k = 50 \text{ m}^{-1}$) in fig. 11.

3.3. BeTSSI Model 3

The BeTSSI model 3 is illustrated in fig. 12. The model is strictly speaking neither convex nor smooth (G^1) due to the attachment of the smaller hemispherical cap to the intermediate cone shape, so this has been taken into account when constructing the artificial boundary. Some meshes are visualized in figs. 13 and 14

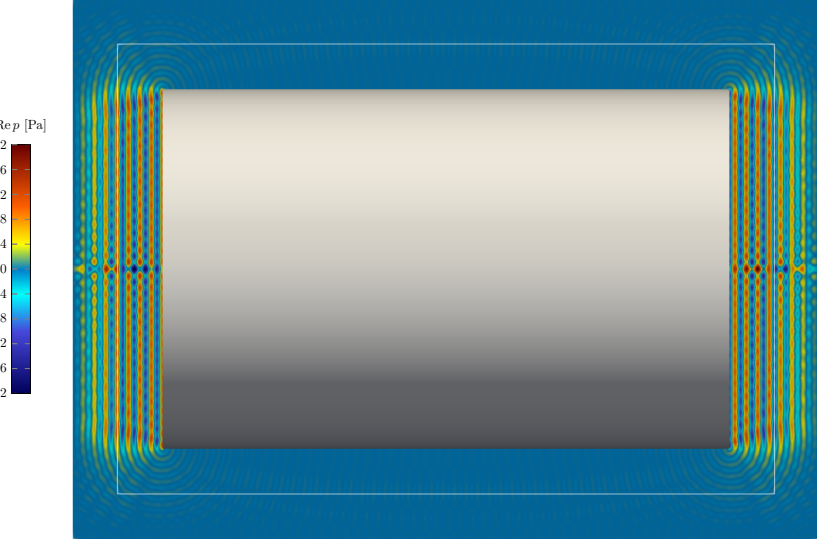


Figure 10: **Scattering from cylinder**: The figure show the scattered near field at $k = 100 \text{ m}^{-1}$ using mesh $\mathcal{M}_{7,2,1}^{\text{IGAPML}}$. The boundary Γ_a is highlighted with a white line.

(with polynomial order \check{p} and continuity \check{k}), and a result for the case of an $\alpha_s = 240^\circ$ and $\beta_s = 0^\circ$ angle of incidence is illustrated in fig. 15. The far field of the same simulation is plotted in fig. 16 as a function of the aspect angle α . Mesh $\mathcal{M}_{5,2,1}^{\text{IGAPML}}$ is in good agreement with the reference solution (using BEM [18]). Mesh $\mathcal{M}_{6,2,1}^{\text{IGAPML}}$ is visually indistinguishable with the reference solution. Similar results are shown in a monostatic case (with $\alpha_s = \alpha$ and $\beta_s = \beta = 0$) in fig. 17.

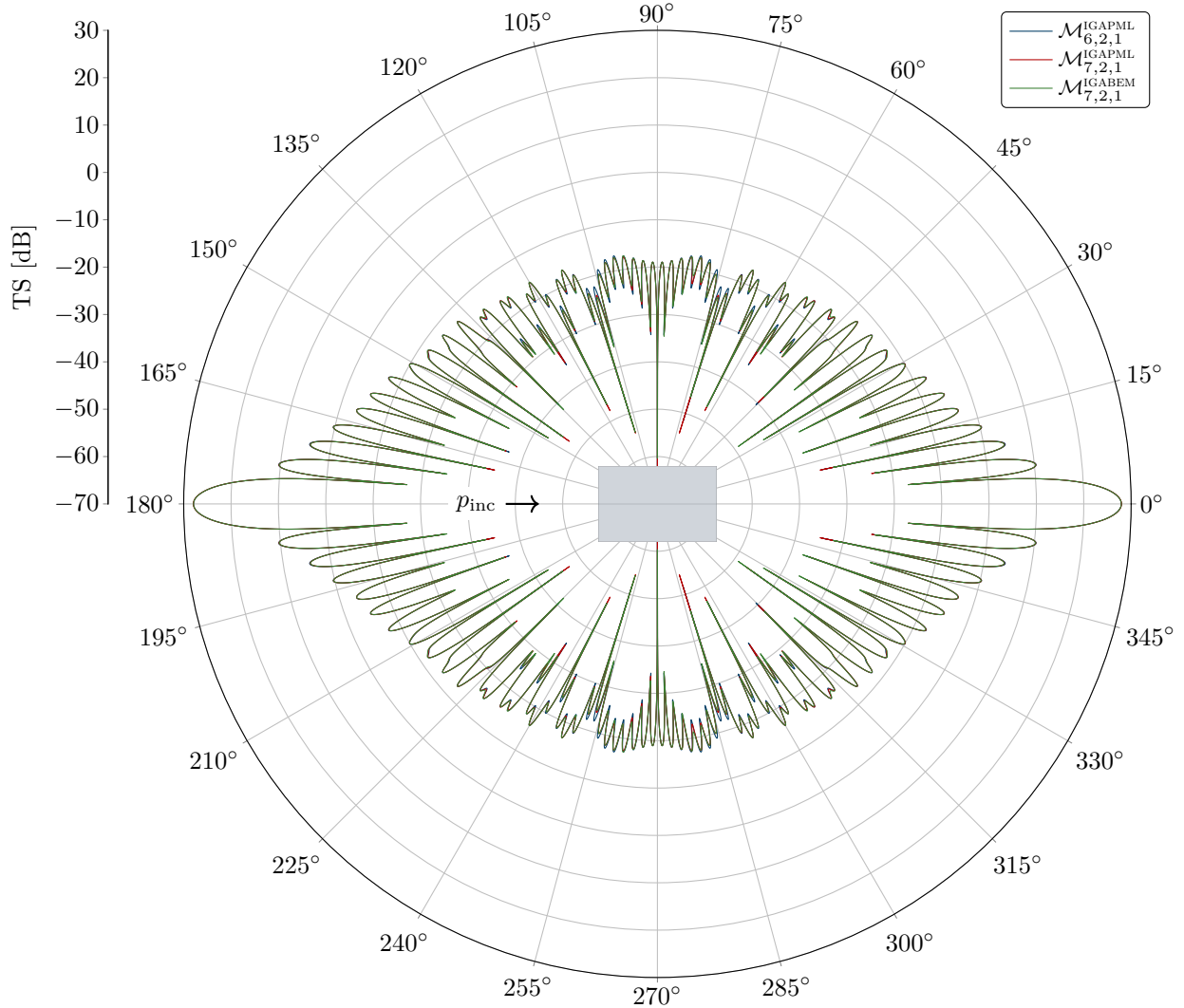


Figure 11: **Scattering from cylinder:** Far field pattern as a function of the aspect angle α at $k = 50 \text{ m}^{-1}$. The CCBIEC formulation was used for the BEM reference solution. The back scattering (at $\alpha = 180^\circ$) and forward scattering (at $\alpha = 0^\circ$) is present as expected.

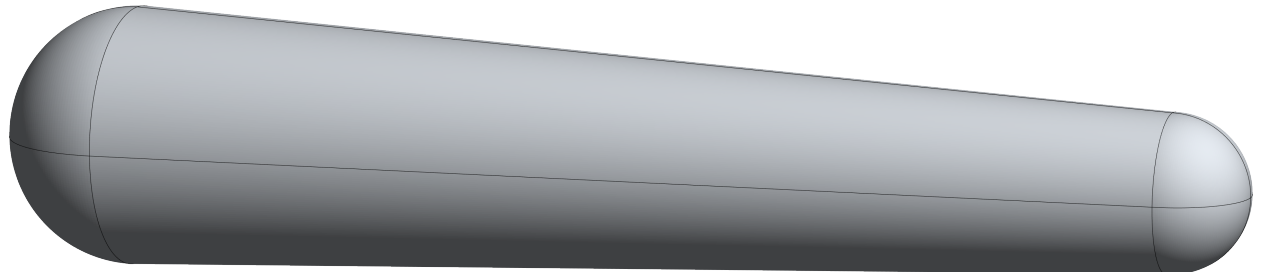


Figure 12: **The BeTSSI model 3:** This model is one of the benchmark models in the BeTSSI (Benchmark Target Strength Simulations [59]) community. The BeTSSI model 3 (M3) is a model given by two hemispherical end caps with radii $R_1 = 3 \text{ m}$ and $R_2 = 5 \text{ m}$ connected by a cone of length $L = 41 \text{ m}$. The speed of sound in the fluid is $c = 1500 \text{ ms}^{-1}$.

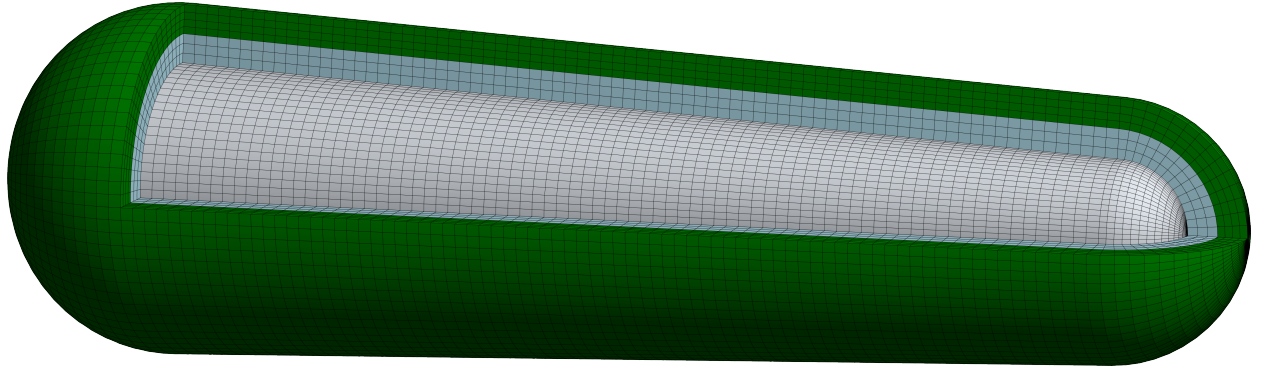


Figure 13: **The BeTSSI model 3:** Mesh $\mathcal{M}_{5,\bar{p},\bar{k}}^{\text{IGAPML}}$ illustrating the perfectly matched layer (green) domain Ω_b around the (light blue) domain Ω_a . The distance to the PML layer is the same as the thickness; $t_{\text{pml}} = 0.25R_2$.

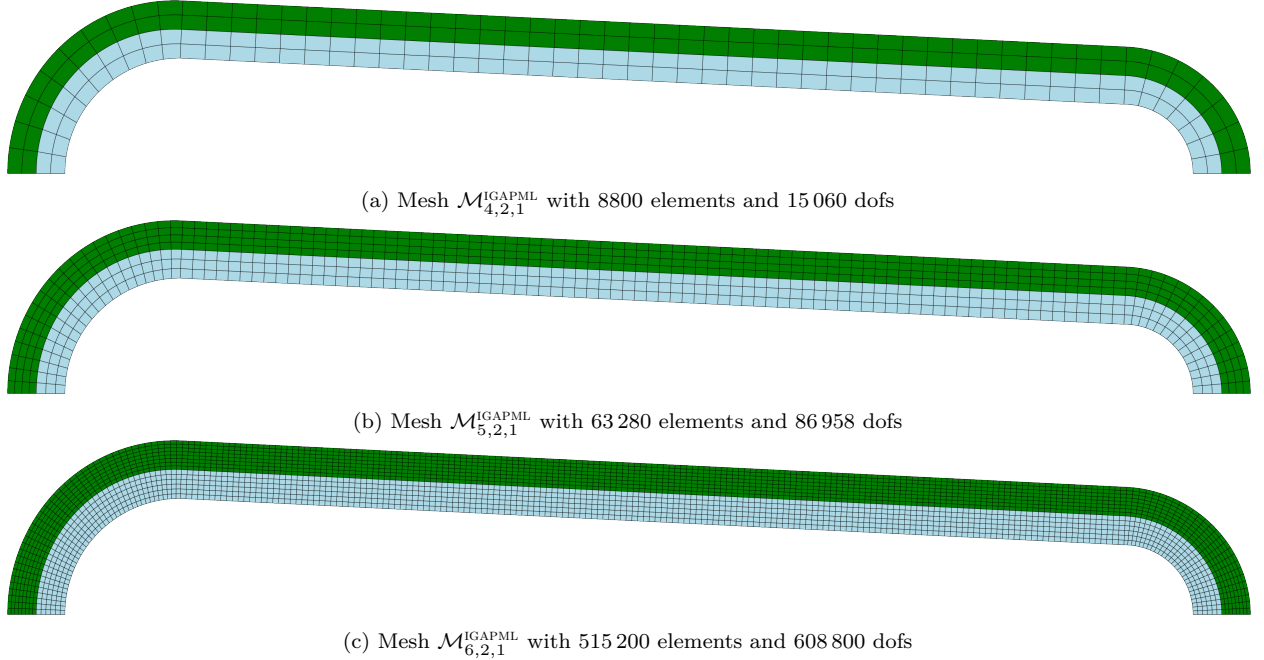


Figure 14: **The BeTSSI model 3:** Illustration of the meshes where the refinement is performed reducing the aspect ratio of the coarse mesh.

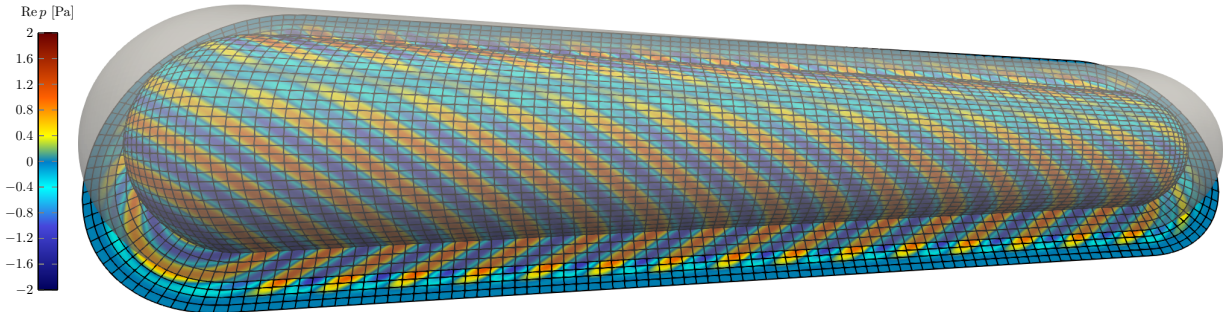


Figure 15: **The BeTSSI model 3:** Results on mesh $\mathcal{M}_{5,2,1}^{\text{IGAPML}}$ illustrating the scattered pressure both in the vicinity of the scatterer and in the PML. The artificial boundary Γ_a is added as a transparent surface.

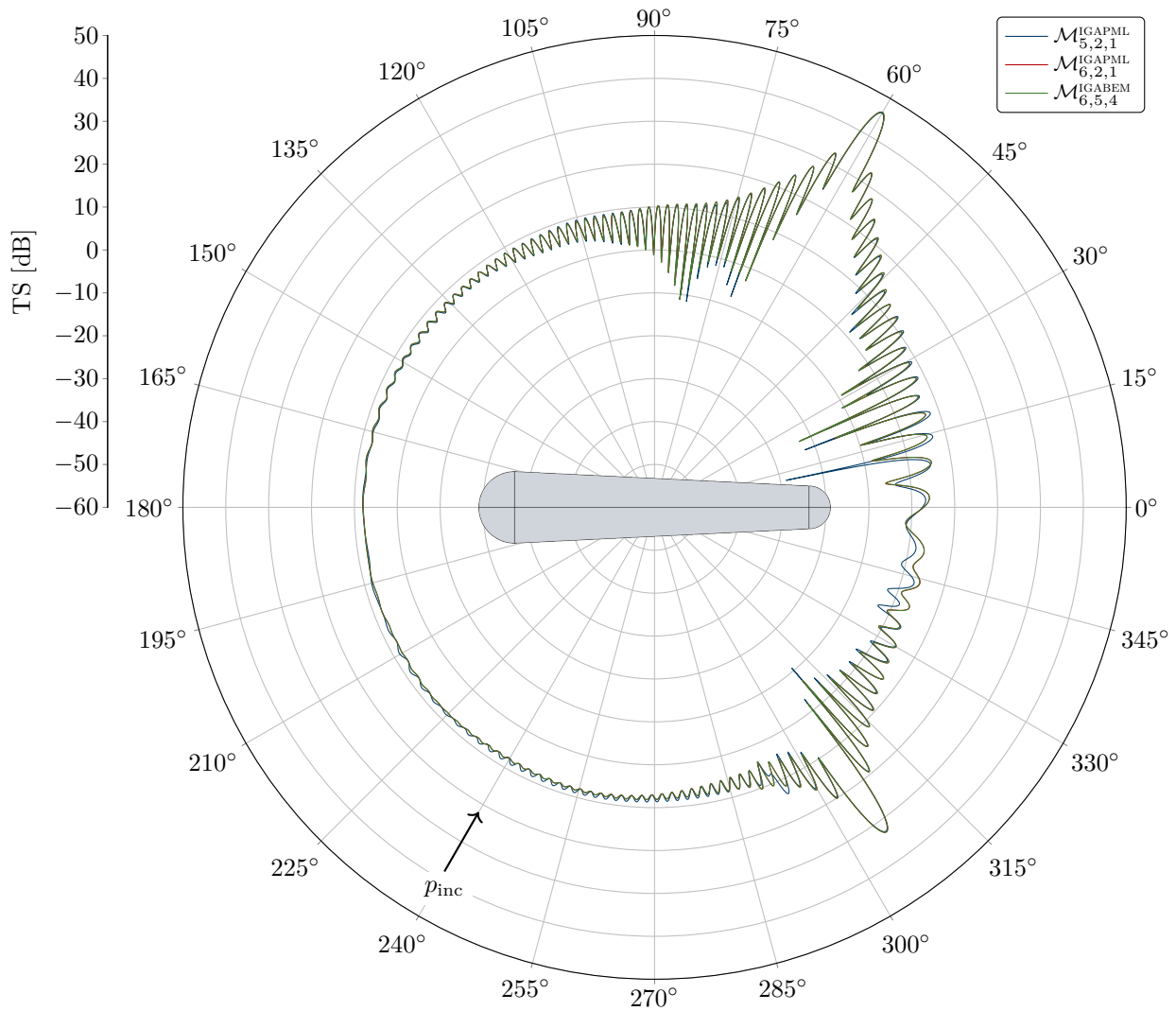


Figure 16: **The BeTSSi model 3:** Far field pattern as a function of the aspect angle α . The CCBIE formulation was used for the BEM reference solution.

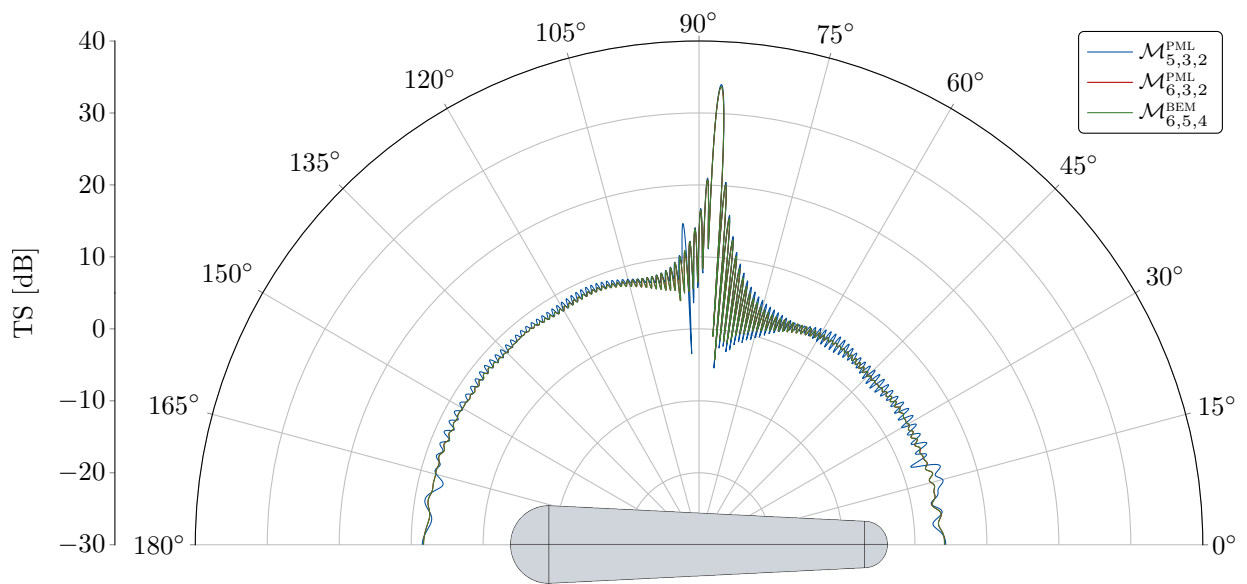


Figure 17: **The BeTSSI model 3:** Far field pattern as a function of the aspect angle α at $f = 1$ kHz.

4. Conclusions

In this work a general spline based PML formulation has been presented to ease the construction of the PML domain. The formulation is no longer dependent on coordinate systems like the cylindrical, ellipsoidal or the Cartesian coordinate system. Instead, it is based directly on the spline space in which the numerical solution is sought. This eliminates calls to trigonometric functions and enables the PML to be truly matched to any convex and smooth artificial boundary. The application to non-smooth artificial boundary could in principle also be implemented in an automatic fashion based on a wedge fill outlined in this work. This is suggested as future work.

Only a modification of the standard Jacobian is needed in the bilinear form instead of several Jacobians from additional coordinate transformations. As restrictions to the computational domains are reduced, both mesh quality and computational efficiency can be improved by the present approach. Moreover, the usage of spline basis function of higher continuity improves accuracy through the IGA framework.

The usage of unbounded absorption function conveniently reduces the number of PML parameters to tune. In the experiments we only need to tune the distance to the artificial boundary and the thickness of the PML layer. For a reasonable distance to the artificial boundary, we have used the same distance as the PML thickness yielding reasonably good results, in which case the PML thickness is the most sensitive parameter to tune for high accuracies. Until pollution from the PML-thickness occurs, the PML approximation yields solution close to the best approximation indicating that the integrations over the unbounded absorption functions are well resolved.

Acknowledgements

This work was supported by SINTEF Digital.

References

- [1] S. A. Sauter, C. Schwab, *Boundary Element Methods*, Springer Berlin Heidelberg, Berlin, Heidelberg, 2011, pp. 183–287.
- [2] M. Schanz, O. Steinbach, *Boundary Element Analysis: Mathematical Aspects and Applications*, Lecture Notes in Applied and Computational Mechanics, Springer Berlin Heidelberg, 2007.
- [3] S. Marburg, B. Nolte, *Computational Acoustics of Noise Propagation in Fluids-Finite and Boundary Element Methods*, vol. 578, Springer, 2008.
- [4] S. N. Chandler-Wilde, I. G. Graham, S. Langdon, E. A. Spence, *Numerical-asymptotic boundary integral methods in high-frequency acoustic scattering*, *Acta Numerica*, 21:89–305 (2012).
- [5] J.-P. Berenger, *A perfectly matched layer for the absorption of electromagnetic waves*, *Journal of Computational Physics*, 114:185–200 (1994).
- [6] J.-P. Berenger, *Perfectly matched layer for the FDTD solution of wave-structure interaction problems*, *IEEE Transactions on Antennas and Propagation*, 44:110–117 (1996).
- [7] P. J. Matuszyk, L. F. Demkowicz, *Parametric finite elements, exact sequences and perfectly matched layers*, *Computational Mechanics*, 51:35–45 (2012).
- [8] D. Givoli, *Numerical methods for problems in infinite domains*, vol. 33, Elsevier, 2013.
- [9] J. J. Shirron, *Solution of exterior Helmholtz problems using finite and infinite elements*, Ph.D. thesis, University of Maryland College Park (1995).
- [10] A. Bayliss, M. Gunzburger, E. Turkel, *Boundary conditions for the numerical solution of elliptic equations in exterior regions*, *SIAM Journal on Applied Mathematics*, 42:430–451 (1982).
- [11] T. Hagstrom, S. Hariharan, *A formulation of asymptotic and exact boundary conditions using local operators*, *Applied Numerical Mathematics*, 27:403–416 (1998), Special Issue on Absorbing Boundary Conditions.
- [12] R. Tezaur, A. Macedo, C. Farhat, R. Djellouli, *Three-dimensional finite element calculations in acoustic scattering using arbitrarily shaped convex artificial boundaries*, *International Journal for Numerical Methods in Engineering*, 53:1461–1476 (2001).
- [13] P. Bettess, *Infinite elements*, *International Journal for Numerical Methods in Engineering*, 11:53–64 (1977).
- [14] P. Bettess, O. C. Zienkiewicz, *Diffraction and refraction of surface waves using finite and infinite elements*, *International Journal for Numerical Methods in Engineering*, 11:1271–1290 (1977).
- [15] L. Demkowicz, F. Ihlenburg, *Analysis of a coupled finite-infinite element method for exterior Helmholtz problems*, *Numerische Mathematik*, 88:43–73 (2001).
- [16] T. Hughes, J. Cottrell, Y. Bazilevs, *Isogeometric analysis: CAD, finite elements, NURBS, exact geometry and mesh refinement*, *Computer Methods in Applied Mechanics and Engineering*, 194:4135–4195 (2005).

[17] J. V. Venås, T. Kvamsdal, T. Jenserud, [Isogeometric analysis of acoustic scattering using infinite elements](#), *Computer Methods in Applied Mechanics and Engineering*, 335:152–193 (2018).

[18] J. V. Venås, T. Kvamsdal, [Isogeometric boundary element method for acoustic scattering by a submarine](#), *Computer Methods in Applied Mechanics and Engineering*, 359:112670 (2020).

[19] R. Simpson, S. Bordas, J. Trevelyan, T. Rabczuk, [A two-dimensional isogeometric boundary element method for elastostatic analysis](#), *Computer Methods in Applied Mechanics and Engineering*, 209–212:87–100 (2012).

[20] R. N. Simpson, M. A. Scott, M. Taus, D. C. Thomas, H. Lian, [Acoustic isogeometric boundary element analysis](#), *Computer Methods in Applied Mechanics and Engineering*, 269:265–290 (2014).

[21] M. Peake, J. Trevelyan, G. Coates, [Extended isogeometric boundary element method \(XIBEM\) for two-dimensional Helmholtz problems](#), *Computer Methods in Applied Mechanics and Engineering*, 259:93–102 (2013).

[22] M. Peake, [Enriched and isogeometric boundary element methods for acoustic wave scattering](#), Ph.D. thesis, Durham University (2014).

[23] M. Peake, J. Trevelyan, G. Coates, [Extended isogeometric boundary element method \(XIBEM\) for three-dimensional medium-wave acoustic scattering problems](#), *Computer Methods in Applied Mechanics and Engineering*, 284:762–780 (2015), Isogeometric Analysis Special Issue.

[24] J. Dölz, H. Harbrecht, M. Peters, [An interpolation-based fast multipole method for higher-order boundary elements on parametric surfaces](#), *International Journal for Numerical Methods in Engineering*, 108:1705–1728 (2016).

[25] L. Coox, O. Atak, D. Vandepitte, W. Desmet, [An isogeometric indirect boundary element method for solving acoustic problems in open-boundary domains](#), *Computer Methods in Applied Mechanics and Engineering*, 316:186–208 (2017).

[26] S. Keuchel, N. C. Hagelstein, O. Zaleski, O. von Estorff, [Evaluation of hypersingular and nearly singular integrals in the isogeometric boundary element method for acoustics](#), *Computer Methods in Applied Mechanics and Engineering*, 325:488–504 (2017).

[27] J. Dölz, H. Harbrecht, S. Kurz, S. Schöps, F. Wolf, [A fast isogeometric BEM for the three dimensional Laplace- and Helmholtz problems](#), *Computer Methods in Applied Mechanics and Engineering*, 330:83–101 (2018).

[28] Y. Sun, J. Trevelyan, G. Hattori, C. Lu, [Discontinuous isogeometric boundary element \(IGABEM\) formulations in 3D automotive acoustics](#), *Engineering Analysis with Boundary Elements*, 105:303–311 (2019).

[29] Y. Wu, C. Dong, H. Yang, [Isogeometric indirect boundary element method for solving the 3D acoustic problems](#), *Journal of Computational and Applied Mathematics*, 363:273–299 (2020).

[30] C. Liu, L. Chen, W. Zhao, H. Chen, [Shape optimization of sound barrier using an isogeometric fast multipole boundary element method in two dimensions](#), *Engineering Analysis with Boundary Elements*, 85:142–157 (2017).

[31] L. Chen, C. Liu, W. Zhao, L. Liu, [An isogeometric approach of two dimensional acoustic design sensitivity analysis and topology optimization analysis for absorbing material distribution](#), *Computer Methods in Applied Mechanics and Engineering*, 336:507–532 (2018).

[32] L. Chen, W. Zhao, C. Liu, H. Chen, S. Marburg, [Isogeometric fast multipole boundary element method based on burton-miller formulation for 3d acoustic problems](#), *Archives of Acoustics*, vol. 44:475–492 (2019).

[33] L. Chen, H. Lian, Z. Liu, H. Chen, E. Atroshchenko, S. Bordas, [Structural shape optimization of three dimensional acoustic problems with isogeometric boundary element methods](#), *Computer Methods in Applied Mechanics and Engineering*, 355:926–951 (2019).

[34] L. Chen, C. Lu, H. Lian, Z. Liu, W. Zhao, S. Li, H. Chen, S. P. Bordas, [Acoustic topology optimization of sound absorbing materials directly from subdivision surfaces with isogeometric boundary element methods](#), *Computer Methods in Applied Mechanics and Engineering*, 362:112806 (2020).

[35] A. M. Shaaban, C. Anitescu, E. Atroshchenko, T. Rabczuk, [Shape optimization by conventional and extended isogeometric boundary element method with PSO for two-dimensional helmholtz acoustic problems](#), *Engineering Analysis with Boundary Elements*, 113:156–169 (2020).

[36] A. M. Shaaban, C. Anitescu, E. Atroshchenko, T. Rabczuk, [Isogeometric boundary element analysis and shape optimization by PSO for 3d axi-symmetric high frequency helmholtz acoustic problems](#), *Journal of Sound and Vibration*, 486:115598 (2020).

[37] A. M. Shaaban, C. Anitescu, E. Atroshchenko, T. Rabczuk, [3d isogeometric boundary element analysis and structural shape optimization for helmholtz acoustic scattering problems](#), *Computer Methods in Applied Mechanics and Engineering*, 384:113950 (2021).

[38] A. M. Shaaban, C. Anitescu, E. Atroshchenko, T. Rabczuk, [An isogeometric burton-miller method for the transmission loss optimization with application to mufflers with internal extended tubes](#), *Applied Acoustics*, 185:108410 (2022).

[39] X. Xie, Y. Liu, [An adaptive model order reduction method for boundary element-based multi-frequency acoustic wave problems](#), *Computer Methods in Applied Mechanics and Engineering*, 373:113532 (2021).

[40] U. Hetmaniuk, R. Tezaur, C. Farhat, [Review and assessment of interpolatory model order reduction methods for frequency response structural dynamics and acoustics problems](#), *International Journal for Numerical Methods in Engineering*, 90:1636–1662 (2012).

[41] U. Hetmaniuk, R. Tezaur, C. Farhat, [An adaptive scheme for a class of interpolatory model reduction methods for frequency response problems](#), *International Journal for Numerical Methods in Engineering*, 93:1109–1124 (2012).

[42] A. Quarteroni, A. Manzoni, F. Negri, *Reduced Basis Methods for Partial Differential Equations: An Introduction*, UNITEXT, Springer International Publishing, 2015.

[43] A. Safjan, M. Newman, [Three-dimensional infinite elements utilizing basis functions with compact support](#), *Computers & Mathematics with Applications*, 43:981–1002 (2002).

[44] H. Bériot, A. Modave, [An automatic perfectly matched layer for acoustic finite element simulations in convex domains of general shape](#), *International Journal for Numerical Methods in Engineering* (2020).

- [45] O. Ozgun, M. Kuzuoglu, [Non-maxwellian locally-conformal PML absorbers for finite element mesh truncation](#), *IEEE Transactions on Antennas and Propagation*, 55:931–937 (2007).
- [46] O. Ozgun, M. Kuzuoglu, [Near-field performance analysis of locally-conformal perfectly matched absorbers via monte carlo simulations](#), *Journal of Computational Physics*, 227:1225–1245 (2007).
- [47] Y. Mi, X. Yu, [Isogeometric locally-conformal perfectly matched layer for time-harmonic acoustics](#), *Computer Methods in Applied Mechanics and Engineering*, 384:113925 (2021).
- [48] D. Drzisga, B. Keith, B. Wohlmuth, [The surrogate matrix methodology: Accelerating isogeometric analysis of waves](#), *Computer Methods in Applied Mechanics and Engineering*, 372:113322 (2020).
- [49] A. Sommerfeld, [Partial differential equations in physics](#), vol. 1, Academic press, 1949.
- [50] F. Ihlenburg, [Finite Element Analysis of Acoustic Scattering](#), vol. 132 of *Applied Mathematical Sciences*, Springer, New York, USA, 1998.
- [51] J. Cottrell, A. Reali, Y. Bazilevs, T. Hughes, [Isogeometric analysis of structural vibrations](#), *Computer Methods in Applied Mechanics and Engineering*, 195:5257–5296 (2006).
- [52] J. J. Shirron, T. E. Giddings, [A finite element model for acoustic scattering from objects near a fluid–fluid interface](#), *Computer Methods in Applied Mechanics and Engineering*, 196:279–288 (2006).
- [53] C. Michler, L. Demkowicz, J. Kurtz, D. Pardo, [Improving the performance of perfectly matched layers by means of *hp*-adaptivity](#), *Numerical Methods for Partial Differential Equations*, 23:832–858 (2007).
- [54] A. V. Astaneh, B. Keith, L. Demkowicz, [On perfectly matched layers for discontinuous Petrov–Galerkin methods](#), *Computational Mechanics*, 63:1131–1145 (2018).
- [55] A. Bermúdez, L. Hervella-Nieto, A. Prieto, R. Rodríguez, [An optimal perfectly matched layer with unbounded absorbing function for time-harmonic acoustic scattering problems](#), *Journal of Computational Physics*, 223:469–488 (2007).
- [56] A. Bermúdez, L. Hervella-Nieto, A. Prieto, R. Rodríguez, [An exact bounded perfectly matched layer for time-harmonic scattering problems](#), *SIAM Journal on Scientific Computing*, 30:312–338 (2008).
- [57] T. W. Wu, A. F. Seybert, [A weighted residual formulation for the CHIEF method in acoustics](#), *The Journal of the Acoustical Society of America*, 90:1608–1614 (1991).
- [58] H. A. Schenck, [Improved integral formulation for acoustic radiation problems](#), *The Journal of the Acoustical Society of America*, 44:41–58 (1968).
- [59] B. Nolte, I. Schäfer, C. de Jong, L. Gilroy, [BeTSSi II benchmark on target strength simulation](#), in *Proceedings of Forum Acusticum*, 2014.